Numerical simulation of the postformation evolution of a laminar vortex ring

Ionut Danaila[1] and Jérôme Hélie[2]

[1]*UPMC Université Paris 06, UMR 7598, Laboratoire Jacques-Louis Lions, F-75005 Paris, France*
[2]*Continental Automotive France, 1 av. Paul Ourliac, BP 1149, F-31036 Toulouse, France*

Direct numerical simulations are used to study the postformation evolution of a laminar vortex ring. The vortex structure is described by calculating the embedded boundaries of the vortex inner core, vortex core, and vortex bubble. The topology of the vortex ring is found to be self-similar during the entire postformation phase. We also show that extracting the vortex inner core provides an objective method in setting the upper value for the cutoff vorticity level separating the vortex from its tail. The computed power laws describing the decay of the translation velocity and integrals of motion (circulation, impulse, and energy) are shown to be consistent with both studies of Dabiri and Gharib [J. Fluid Mech. **511**, 311 (2004)] and Maxworthy [J. Fluid Mech. **51**, 15 (1972)]. We prove that the apparently different scaling laws reported in these two studies collapse if a virtual time origin is properly defined. Finally, the computationally generated vortex rings are matched to the classical Norbury–Fraenkel model and the recent model proposed by Kaplanski and Rudi [Phys. Fluids **17**, 087101 (2005)]. The former model provides not only a good prediction of normalized energy and circulation but also a good estimation of individual integrals of motion. The latter model offers, in addition to a good prediction of integral quantities, a more accurate description of the vortex ring topology when comparing the contours of the inner cores or vortex signatures. Both models underestimate the volume of fluid carried inside the vortex bubble. © *2008 American Institute of Physics*. [DOI: 10.1063/1.2949286]

I. INTRODUCTION

The fundamental and practical interest of the scientific community in vortex rings has generated a large volume of literature for at least a hundred years (see the reviews by Shariff and Leonard,[1] and Lim and Nickels[2]). The present work focuses on the postformation evolution of a laminar vortex ring and is motivated by two recent contributions on this topic, made by Dabiri and Gharib[3] and, respectively, by Kaplanski and Rudi.[4] The former used a new experimental technique to measure vortex ring entrainment and reported scaling laws for the main integrals of motion different from those established by Maxworthy[5] in 1972 and currently used in the literature. The latter proposed a more realistic model than the commonly used Norbury–Fraenkel[6,7] model to describe the postformation vortex ring. The purpose of this paper is to numerically investigate the scaling laws and geometric parameters characterizing the postformation evolution of a vortex ring. We also address the more general question of how to fit the properties of a numerically (or experimentally) generated vortex ring to ideal vortex ring models.

Laminar vortex rings are usually generated in laboratory by a piston/cylinder arrangement sketched in Fig. 1. A column of fluid is pushed by a piston into a quiescent surrounding. The boundary layer at the edge of the cylinder separates and rolls up into a vortex ring. The flow is assumed to be axisymmetric and thus easily described in cylindrical coordinates (r,z). The main integrals of motion are the circulation (Γ), the hydrodynamic impulse (I), and the energy (E), defined for the case of axisymmetric motion as[8]

$$\Gamma = \int \omega dr dz, \quad I = \pi \int \omega r^2 dr dz, \quad E = \pi \int \omega \psi dr dz,$$

(1)

where ω is the (azimuthal) vorticity and ψ the corresponding Stokes stream function.

A simplified description of the formation process considers that the velocity across the exit plane of the generator of diameter D_p is constant and equal to the average velocity W_p of the piston. The corresponding characteristic time of the process is therefore defined as D_p/W_p. The piston stroke L_p determines the duration of the fluid discharge, taking place for nondimensional times $0 \le W_p t/D_p \le L_p/D_p$.

After the piston stops, the vortex ring continues to entrain surrounding irrotational fluid and a part of its wake. At later times, a vortex bubble is formed ($\partial\Omega_b$ in Fig. 1) defined by the dividing streamline ($\psi_{vr}=0$) and the forward (A) and, respectively, rearward (B) stagnation points. This closed volume of the vortex ring is also called vortex atmosphere.[9] Inside the vortex atmosphere, the fluid circulates over closed streamlines. The vortex ring has the shape of an oblate ellipsoid of revolution, with the vorticity concentrated in the vortex core $\partial\Omega_c$. In the meridional section of the vortex, the vorticity has approximately Gaussian distribution[10,11] with the maximum at the core center (C) of coordinates (R_c, Z_c). The vortex ring translates with its own induced velocity W_v.

An important progress in understanding the behavior of the vortex ring during the formation phase was made by Gharib *et al.*[12] They experimentally showed that for large
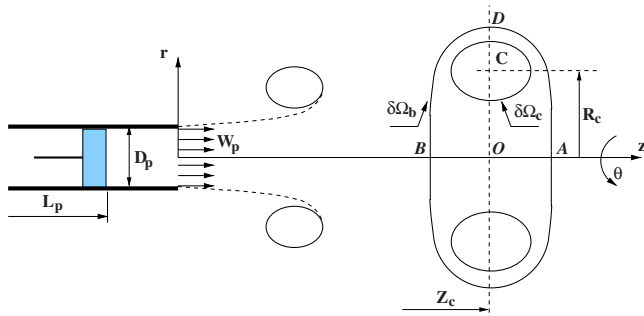
FIG. 1. (Color online) Sketch of the formation of a vortex ring generated by a piston/cylinder arrangement and geometric parameters of the ring during the postformation phase.

stroke ratios $t_p = L_p/D_p > 4$, only a limited amount of the circulation delivered by the discharging flow is engulfed by the vortex ring. The maximum circulation that the vortex ring can attain is produced by the apparatus at a critical time $t_f < t_p$, referred as the "formation number." Any additional circulation generated at the inlet ends up in a trailing jet. The formation number value was reported to range from 3.6 to 4.5 for a variety of exit diameters, exit geometries, and piston velocity moving programs. The investigation of the universality of the formation time has focused the effort of most recent experimental,[12–14] numerical,[15–17] and theoretical[18–21] studies. The formation time is presumed to have a major importance in practical applications (e.g., propulsion and locomotion of biological systems, injection in internal combustion engines).

The evolution of the vortex ring during the postformation phase was, in exchange, less investigated by means of modern experimental and numerical techniques. The reference work on the diffusive evolution of the vortex ring goes back to the 1970s, when Maxworthy[5,22] experimentally and theoretically established the scaling laws for the main integrals of motion. He reported a −1 power-law decay for the translational vortex ring velocity ($W_v \sim t^{-1}$) and a −2/3 power-law decay for the vortex ring circulation ($\Gamma_v \sim t^{-2/3}$). He also predicted a −1/3 power law for the circulation of the entire flow field (vortex bubble and its wake). This analysis was performed assuming the impulse of the vortex bubble to be a constant. In recent experiments of Dabiri and Gharib[3] (henceforth denoted as DG) much smaller decay rates were measured: $W_v \sim t^{-1/3}$ and $\Gamma_v \sim t^{-p}$, with $p = 0.15$ or $p = 0.27$, depending on the stroke ratio. The source of discrepancy in these results was believed to lie in the configuration of the apparatus generating the vortex ring (Maxworthy used a sharp-edged orifice and DG a piston/cylinder arrangement) and in the Reynolds number of the flow, $\text{Re} = W_p D_p / \nu$. Since the scaling law predictions of Maxworthy[5] are admittedly limited to large Reynolds numbers, it was believed that the Reynolds number in experiments of DG was too small (Re $= 1400$). However, Maxworthy's scaling law for the circulation was confirmed in numerical simulations of James and Madnia[23] for a vortex ring generated at Re $= 300$. It is the first objective of this contribution to numerically investigate the scaling laws characterizing the postformation evolution of the vortex ring.

Another important question concerning the vortex ring postformation is how to fit the characteristics of an experimentally or numerically generated vortex ring to those of an ideal model. This is the first step of analytical models predicting the value of the formation time.[4,12,18,19,21] The idea behind these theories is to match the values of the circulation (Γ_p), impulse (I_p), and kinetic energy (E_p) of the discharged fluid to the corresponding values (Γ_v, I_v, E_v) of the vortex ring after the formation phase. The maximum plug length characterizing the formation time is finally predicted using an additional constraint imposed either by equating the translational velocity of the vortex ring by the one predicted by the slug model[18,24] ($W_v \approx W_p/2$) or by matching the volume of the plug to that of the vortex ring.[21]

The ideal vortex ring model of Norbury and Fraenkel[6,7] remains popular to describe the postformation vortex ring evolution. Vortices of this family are identified by a single geometric parameter calculated by equating either the normalized energy[12,17–19,21] or normalized circulation[17,18] of the experimental or numerical vortex ring,

$$E_v^* = E_v/(I_v^{1/2}\Gamma_v^{3/2}), \quad \Gamma_v^* = \Gamma_v/(I_v^{1/3}W_v^{2/3}), \quad (2)$$

to the corresponding values from the theoretical model. It was found that normalized quantities predicted by the model follow closely the experimental or numerical values. This might be surprising since the hypotheses used in deriving this family of vortices are far from being realistic: the vorticity distribution is linear and the dynamics is inviscid. Kaplanski and Rudi[4] derived a more realistic vortex ring model by taking into account the viscosity and a Gaussian vorticity distribution in the core. Their model was used to successfully predict the value of the formation number, but, to our knowledge, a detailed numerical validation of its predictions has not yet been provided.

The second objective of this paper is therefore to numerically evaluate the validity of ideal vortex ring models in describing not only the evolution of normalized energy and circulation, but also of individual quantities (Γ_v, I_v, W_v). We also compare geometric characteristics such as the core size, the shape, and the volume of the vortex bubble, the position of the vortex center, etc. These geometric details, which are absent in previous studies, may be very useful in modeling phenomena occurring in practical application. One of these is the ignition of a combustible mixture, when the ignition kernel is the vortex ring that forms at the head of the injected transient jet.

II. NUMERICAL AND PHYSICAL PARAMETERS

We integrate the incompressible Navier–Stokes equations in cylindrical coordinates (r, θ, z) using the numerical method proposed by Verzicco and Orlandi.[25] Since this method is described in great detail by Orlandi,[26] we outline here only its main characteristics. The equations are written in primitive variables $(r \cdot v_r, v_\theta, v_z)$ and solved on a staggered grid to avoid the problem of singularities introduced by the axis $r = 0$. Second order finite differences are used for the spatial discretization. For the time advancement we use a fractional-step method[27] based on a combination of a low-

storage third-order Runge–Kutta scheme for the convective terms and a semi-implicit Crank–Nicolson scheme for the viscous terms. At each substep of the Runge–Kutta scheme, the momentum equations are solved by an approximate factorization technique and a Poisson equation is solved for the pressure correction. The Poisson solver uses a fast Fourier transform following the azimuthal direction θ and an effective cyclic reduction method (Fishpack subroutines) for solving the remaining two-dimensional system following (r,z) directions. The method is globally second order accurate in space and time.

For the purpose of this paper, we perform axisymmetric direct numerical simulations of the laminar vortex ring. The piston/cylinder vortex generator can be numerically modeled either by simulating the flow in the cylinder[28] or by prescribing the axial velocity profile at the inflow boundary.[15–17,23] We adopt the second method and specify at the inlet ($z=0$) a discharge velocity profile varying in time and space,

$$V_z(t,r) = V_0(t)V_{zb}(r), \tag{3}$$

where $V_0(t)$ is the "velocity program" proposed by James and Madnia[23] to describe the piston motion,

$$V_0(t) = \begin{cases} \dfrac{W_p}{2}\left\{1 + \tanh\left[\dfrac{5}{\tau_1}(t - \tau_1)\right]\right\}, \\ \quad t \le \tau_1 + \tau_2/2 \\ \dfrac{W_p}{2}\left\{1 + \tanh\left[\dfrac{5}{\tau_1}(\tau_1 + \tau_2 - t)\right]\right\}, \\ \quad t > \tau_1 + \tau_2/2, \end{cases} \tag{4}$$

and V_{zb} is the classical hyperbolic tangent profile, which matches very well the shape of profiles measured in experiments (see, e.g., Michalke[29]),

$$V_{zb}(r) = \frac{1}{2}\left\{1 + \tanh\left[\frac{1}{2\delta_\omega}\left(\frac{D_p}{2r} - \frac{2r}{D_p}\right)\right]\right\}. \tag{5}$$

The parameter δ_ω is the dimensionless thickness of the vorticity layer at the inlet, i.e., $\delta_\omega = W_p D_p / \|\partial V_z/\partial r\|_{max}$. The constants τ_1 and τ_2 separate the three parts in the piston motion: acceleration for $t \in [0, \tau_1)$, velocity plateau $V_0 = W_p$ for $t \in]\tau_1, \tau_2]$ and deceleration for $t \in]\tau_2, t_{off}]$. At t_{off} the axial velocity becomes zero in the entire inlet section. The injected plug is usually described using the so-called slug model,[1,2] assuming that near the exit plane of the vortex generator the flow is parallel and characterized by a top-hat velocity profile (see Fig. 1). It follows that the stroke length (L_p), circulation (Γ_p), impulse (I_p), and kinetic energy (E_p) of the discharged fluid at the cylinder lip are calculated as

$$L_p = \int_0^{t_{off}} V_0(\tau)d\tau, \quad \Gamma_p = \frac{1}{2}\int_0^{t_{off}} V_0^2(\tau)d\tau, \tag{6}$$

$$I_p = \frac{\pi D_p^2}{4}\int_0^{t_{off}} V_0^2(\tau)d\tau, \quad E_p = \frac{\pi D_p^2}{8}\int_0^{t_{off}} V_0^3(\tau)d\tau. \tag{7}$$

In the following, all presented quantities will be normalized using the characteristic length D_p, velocity W_p, and time D_p/W_p.

TABLE I. Numerical parameters for the injection programs and corresponding integral quantities evaluated using slug-model equations (6) and (7).

L_p/D_p	τ_1	τ_2	t_{off}	Γ_p	I_p	E_p	E_p^*
2	0.15	2.0	2.29	0.98	1.55	0.77	0.63
4	0.15	4.0	4.29	1.98	3.12	1.55	0.31
6	0.15	6.0	6.29	2.98	4.69	2.34	0.21

Physical parameters of simulations are set accordingly to experiments of DG: the Reynolds number is Re$=1400$ and the stroke ratio is $L_p/D_p=2$ or 4. A third stroke ratio $L_p/D_p=6$ is considered in order to extend our analysis to a case with well-defined vortex pinch-off. The impulsive motion of the piston is modeled by setting short-time acceleration/deceleration phases ($\tau_1=0.15$). The value of the parameter τ_2 is determined by the stroke ratio ($\tau_2 \approx L_p/D_p$). We consider in our simulations a thin vorticity layer at the inlet with $\delta_\omega=0.05$. All parameters describing the injection programs used in present simulations are summarized in Table I.

In order to follow the vortex ring for a long time period ($t \le 40$) for all considered stroke ratios, the axial extent of the computational domain is set to $20D_p$. This allows to avoid vortex ring getting close to the downstream boundary [$\max(Z_c) \le 16D_p$], where we apply a convective[30] boundary condition, enforced by a global mass conservation procedure.[31] The domain extends radially to $r_{max}=4D_p$, which ensures a negligible influence of lateral slip-wall boundary on the dynamics of the vortex ring. In the following, we present high resolution simulations employing 301 $\times$ 1251 grid points. The grid is uniform in the axial direction and stretched in the radial direction such that at least 30 grid points are clustered in the vorticity layer of the inflow axial velocity profile. Computation with higher spatial resolutions confirmed the grid independence of the results.

III. POSTFORMATION EVOLUTION OF THE VORTEX RING

A typical evolution of the vortex ring during the entire numerical simulation is presented in Fig. 2 for the case $L_p/D_p=6$. The total circulation Γ is obtained from Eq. (1) by integrating the vorticity over the entire computational domain, excepting a small region near the inlet ($z \le 0.2$). This eliminates the negative vorticity developing in the inlet wall boundary layer and allows comparison with numerical results of Zhao et al.[16] and experimental data of Gharib et al.[12] Good agreement with both numerical and experimental data is observed.

Figures 2(b)–2(d) show some typical snapshots of the normalized vorticity field ($\tilde{\omega} = \omega/\omega_{max}$). In order to estimate the formation time, we separate the leading vortex ring from the flow using the contour line $\tilde{\omega}=0.05$ (see also the next section). When the separation is not well defined (e.g., $t=10$, $t=15.4$), this contour line is truncated and closed at the downstream location of the center of the vortex ($z=Z_c$). The resulting domains, represented by gray patches in Figs. 2(b)–2(d), are used to compute the vortex ring circulation.
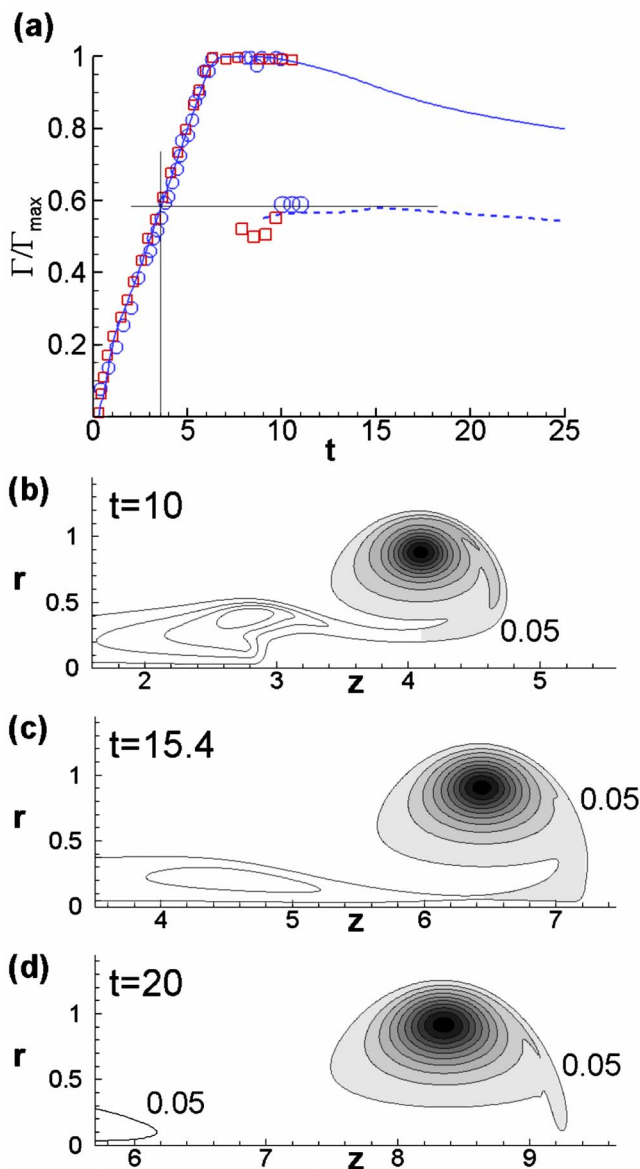
FIG. 2. (Color online) Simulation for $L_p/D_p=6$. (a) Time evolution of the total (solid line) and vortex ring (dashed line) circulation normalized by the maximum value ($\Gamma_{max}=3.27$). Symbols are extracted from Fig. 7 of Zhao *et al.* (Ref. 16); ($\bigcirc$) experimental data of Gharib *et al.* (Ref. 12); ($\square$) numerical result of Zhao *et al.* (Ref. 16). (b)–(d) Contour lines (min=0.05, max=0.95, increment=0.05) of normalized vorticity ($\tilde{\omega}=\omega/\omega_{max}$) before ($t=10$), close to ($t=15.4$), and after ($t=20$) the pinch-off of the vortex ring from its tail. The gray patches are used to compute the circulation of the leading vortex ring.

The pinch-off of the vortex ring is defined to occur[15] when the contour line $\tilde{\omega}=0.05$ encircles the vortex for the first time. A clear pinch-off is observed in our simulations starting from $t=15.4$, a value consistent with previous numerical results.[15,28] Figure 2(a) shows that the circulation of the vortex ring reaches its maximum at the pinch-off time. We infer from the same figure that the formation time at which the total circulation delivered by the vortex generator is equal to the circulation of the pinched-off vortex ring is approximately 3.6. An identical value was experimentally[12] and numerically[15] obtained for similar configurations of the vortex generator.
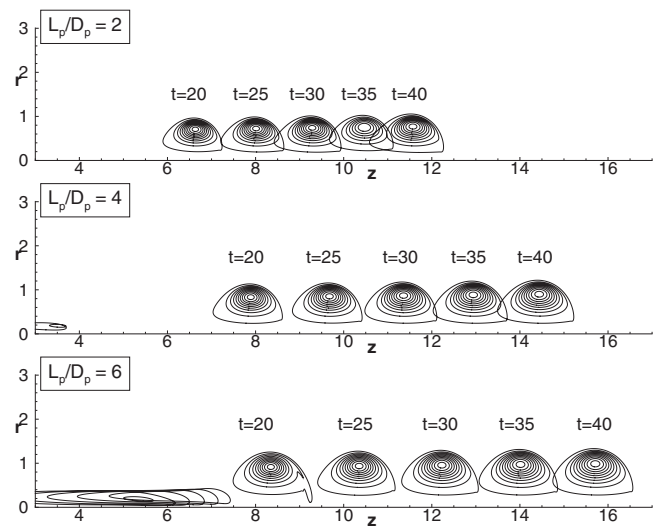

FIG. 3. Evolution of the normalized vorticity field ($\tilde{\omega}$) during the postformation phase for different stroke ratios L_p/D_p (contour lines: min=0.05, max=0.95, increment=0.1).

It seems reasonable to consider that the postformation phase of the vortex ring starts right after the pinch-off. Nevertheless, a well-defined ellipsoidal shape, appropriate to compare results to theoretical predictions, is observed at later times. We note from Fig. 2(d) that a small kink of the lowest vorticity contour is still present at $t=20$. For $t>20$, vorticity contours displayed in Fig. 3 show vortex rings of ellipsoidal shape for all considered stroke ratios. As expected from the estimated value of the formation time ($t_F=3.6$), the trailing jet is absent for $L_p/D_p=2<t_F$ and reduced to a very weak vorticity tail for the stroke ratio $L_p/D_p=4$. The pinch-off in this latter case occurs earlier than for $L_p/D_p=6$, a result already reported by Rosenfeld *et al.*[15] Following these observations, our analysis of the postformation phase will consider vortex ring evolution for $20<t\leqslant40$.

A. Vortex structure: Vortex core, inner core, and bubble

The difficulty in calculating the integrals of motion (Γ_v, I_v, E_v) and geometric characteristics of the vortex ring is to properly separate the leading vortex from its tail. Since the vorticity distribution is approximately Gaussian with the maximum (ω_{max}) in the center (C) of the vortex (see Fig. 1), the generally used method consists in truncating the vorticity field at an *ad hoc* low value. The vortex core ($\delta\Omega_c$) is thus identified as the region of normalized vorticity $\tilde{\omega}=\omega/\omega_{max}>\tilde{\omega}_{cut}$. This corresponds to the intuitive definition of the core as the region concentrating most of the vorticity. Of course, the core is not in practice well defined and the cutoff level is set to the best appreciation of the authors. The values of $\tilde{\omega}_{cut}$, when reported, range from 2% (Ref. 17) and 5% (Refs. 15, 16, and 28) in numerical studies, to approximately 10% (Ref. 3) in experiments.

In the following, we suggest a more objective way to set the cutoff level $\tilde{\omega}_{cut}$. The idea is to use the notion of "inner core radius" introduced by Saffman[32] and defined as the radius measured from the center C of the vortex at which the
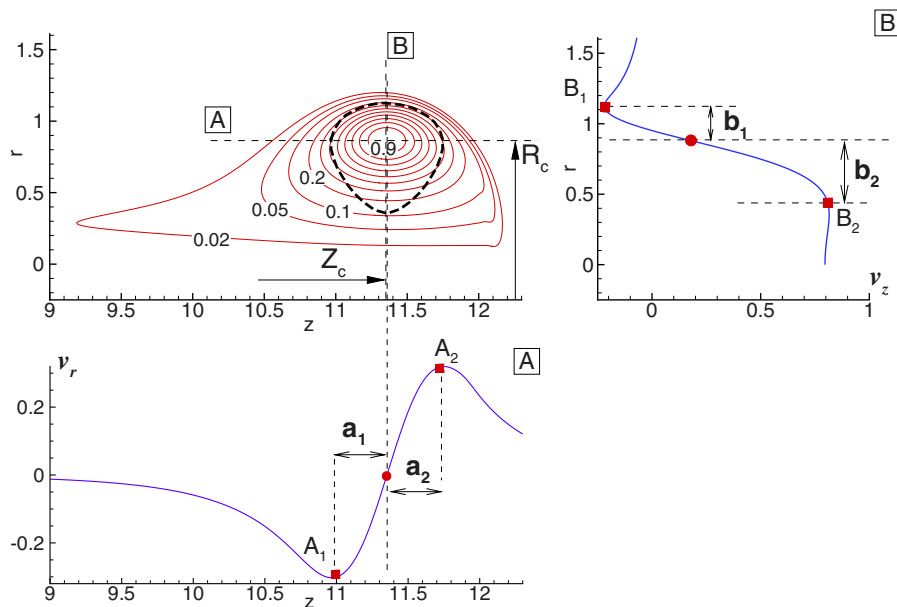
FIG. 4. (Color online) Simulation for $L_p/D_p=4$. Normalized vorticity field $\tilde{\omega}=\omega/\omega_{max}$ at $t=30$. The dashed thick line represents the boundary of the inner core calculated as the locus of points at which the local tangential velocity is maximum. Velocity profiles through the center of the vortex: $v_z(r,Z_c)$ (cut line B) and $v_r(R_c,z)$ (cut line A).

local tangential velocity has its maximum. It is obvious that for a circular vortex with uniform vorticity distribution, the core coincides with the inner core. It is also the case for Hill's spherical vortex and, more generally, for Norbury–Fraenkel's vortex rings (see next sections). This definition was intuitively used in experimental studies of Sullivan[10] and Akhmetov[9] to calculate the dimensions of the core following axial and radial directions. Requesting that the truncated vorticity field includes the inner core will allow to calculate an upper bound $\tilde{\omega}_{cut}^{max}$ for the cutoff value. We illustrate this method by considering the case $L_p/D_p=4$ for which the vortex ring separates earlier.

Figure 4 shows the normalized vorticity field $\tilde{\omega}$ at $t=30$. We can already observe that the isocontour level $\tilde{\omega}=0.02$ is more elongated than the others, including a part of the vortex ring tail. Following the approach used in experiments,[9,10] we now extract velocity profiles following axial and transverse sections through the center of the vortex. The center (C) of the vortex is located at $R_c=0.87$ and $Z_c=11.35$. We plot one-dimensional profiles $v_z(r,Z_c)$ (cut line B) and $v_r(R_c,z)$ (cut line A) that correspond to tangential velocities in the frame of reference centered in (C). The peaks (A_1,A_2) and (B_1,B_2) of these profiles define the radial and, respectively, axial extents of the inner core. If we measure the distances a_1,a_2 and b_1,b_2 (see Fig. 4) and normalize them with the vortex ring radius R_c, we notice that the center of the vortex is located at approximately half the distance between A_1 and A_2 $(a_1/R_c\approx a_2/R_c=0.45)$, while there is a strong asymmetry in the radial direction since $b_1/R_c=0.29$ and $b_2/R_c=0.59$. These ratios indicate that the vortex ring has a relatively thick inner core, but not as thick as Hill's vortex for which the ratio between the core radius and the vortex radius is $\sqrt{2}$. Note that similar vortex structures can be seen in Fig. 6 of Mohseni *et al.*,[17] displaying numerically generated vortex rings by applying nonconservative forces of long duration.

The complete contour $\delta\Omega_{ic}$ of the inner core is calculated using the same procedure. Velocity profiles along 36 radii

starting from the center of the vortex at angles covering uniformly $[0,2\pi]$ are extracted from the flow field by a bicubic interpolation procedure. For each radial direction, the point corresponding to the maximum of the tangential velocity (in the frame of reference attached to the vortex center) is located and finally used to draw the inner core. The contour of the inner core is superimposed to vorticity isocontours in Fig. 4 and plotted separately in Fig. 5 for different time instants. The shape of the inner core is different from the generally admitted circular one[9,10] and remains remarkably similar during the postformation phase if we use normalized local coordinates $(r_0/R_c, z_0/R_c)$ in the frame of reference attached to the center of the vortex.

It is interesting to follow the evolution in time of the dimensions of the inner core. Figure 6 shows that the axial symmetry is kept $(a_1\approx a_2)$ while the inner core becomes more elongated in the radial direction, since b_1 is almost constant and b_2 increases (see also Fig. 5). This is a direct consequence of the increase of the vortex ring radius R_c during the postformation phase. We now monitor the minimum value of the normalized vorticity contained in the inner core.
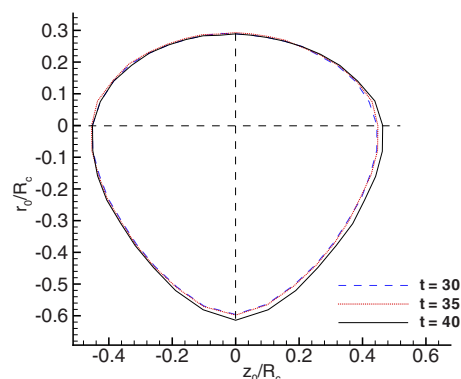

FIG. 5. (Color online) Simulation for $L_p/D_p=4$. Contour of the inner core for different time instants. Local normalized coordinates $(r_0/R_c, z_0/R_c)$ in the frame of reference attached to the center of the vortex.
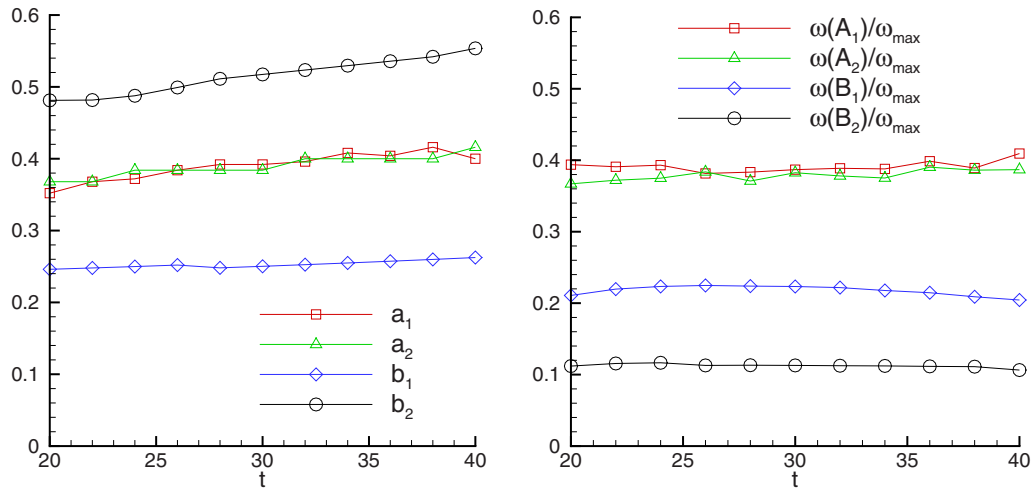
FIG. 6. (Color online) Simulation for $L_p/D_p=4$. Variation in time of the axial (a_1,a_2) and radial dimensions (b_1,b_2) of the inner core and normalized vorticity corresponding to points A_1, A_2, B_1, and B_2 (see Fig. 4 for definitions).

Figure 6 also shows that the point B_2, which is the closest to the axis, sets this minimum value to approximately 0.10. Consequently, the criterion of including the inner core in the truncated vorticity field imposes that $\tilde{\omega}_{cut} \lesssim 0.1$. For the other considered stroke ratios, we obtain $\tilde{\omega}_{cut}^{max}=0.08$ for $L_p/D_p=2$ and $\tilde{\omega}_{cut}^{max}=0.13$ for $L_p/D_p=6$. In the next section, when calculating the integrals of motion, we shall set $\tilde{\omega}_{cut}=0.05$, a value satisfying our criterion for all stroke ratios.

Since in theoretical models the vorticity is zero outside the vortex core, we can assimilate the core of the simulated vortex ring to the simply connected surface $\Omega_c=\{\tilde{\omega} \geqslant \tilde{\omega}_{cut} =0.05\}$ that has the vortex center C as an inner point. In other words, the boundary $\delta\Omega_c$ is the closed isocontour curve $\tilde{\omega}=0.05$ that encircles the center C (see Fig. 7).

The truncated vorticity field is used to calculate the stream function ψ in the laboratory frame by inverting the elliptic equation

$$\frac{\partial^2 \psi}{\partial z^2} + \frac{\partial^2 \psi}{\partial r^2} - \frac{1}{r}\frac{\partial \psi}{\partial r} = -r\omega \qquad (8)$$

using the same solver as in the Navier–Stokes code. Dirichlet conditions are calculated from the velocity field at the boundaries, and particular care is devoted to the treatment of the singularities introduced by the axis $(r=0)$. The stream function in the reference frame moving with the vortex ring is finally calculated as

$$\psi_{vr} = \psi - \frac{1}{2}r^2 W_v, \qquad (9)$$

with the translational velocity estimated by tracking the position of the vortex center $W_v=dZ_c/dt$. The dividing streamline $\psi_{vr}=0$ sets the contour of the vortex bubble $\delta\Omega_b$. The structure of the vortex ring sketched in Fig. 1 can be now plotted more precisely. Figure 7(a) displays the contours of the vortex core, inner core, and vortex bubble for the case $L_p/D_p=4$, $t=30$. This structure remains similar during the postformation evolution of the vortex ring. The areas of the inner core and vortex core increase slowly in time, but the area ratios [see Fig. 7(b)] are remarkably constant for $t>25$ ($|\Omega_c|/|\Omega_b| \approx 0.54$ and $|\Omega_{ic}|/|\Omega_b|=0.2$). These area ratios slightly decrease with the stroke ratio L_p/D_p.

B. Scaling laws for the integrals of motion

The main integrals of motion (Γ_v, I_v, E_v) for the vortex ring evolution during the postformation phase are calculated using the formulas (1). The integrals are numerically computed over the vortex core domain Ω_c defined previously. Notice that Ω_c is varying with time.
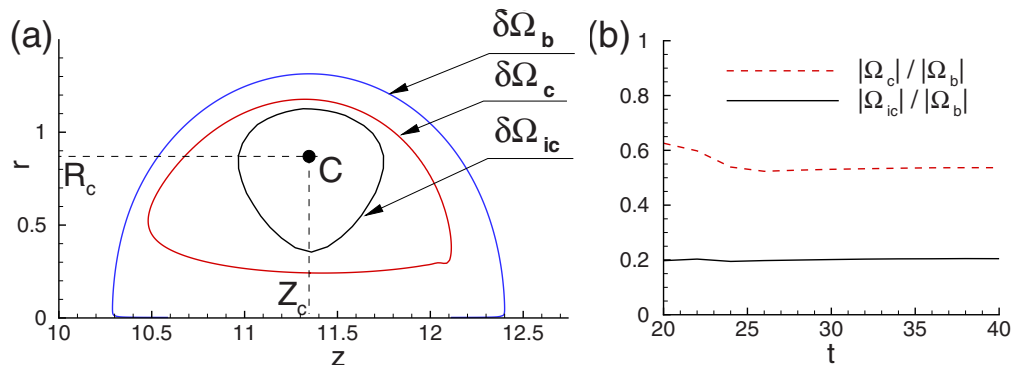

FIG. 7. (Color online) Simulation for $L_p/D_p=4$. (a) Contours of the inner core $(\delta\Omega_{ic})$, vortex core $(\delta\Omega_c)$, and vortex bubble $(\delta\Omega_b)$ at $t=30$. (b) Variation in time of the area ratios $|\Omega_c|/|\Omega_b|$ (dashed line) and $|\Omega_{ic}|/|\Omega_b|$ (solid line).
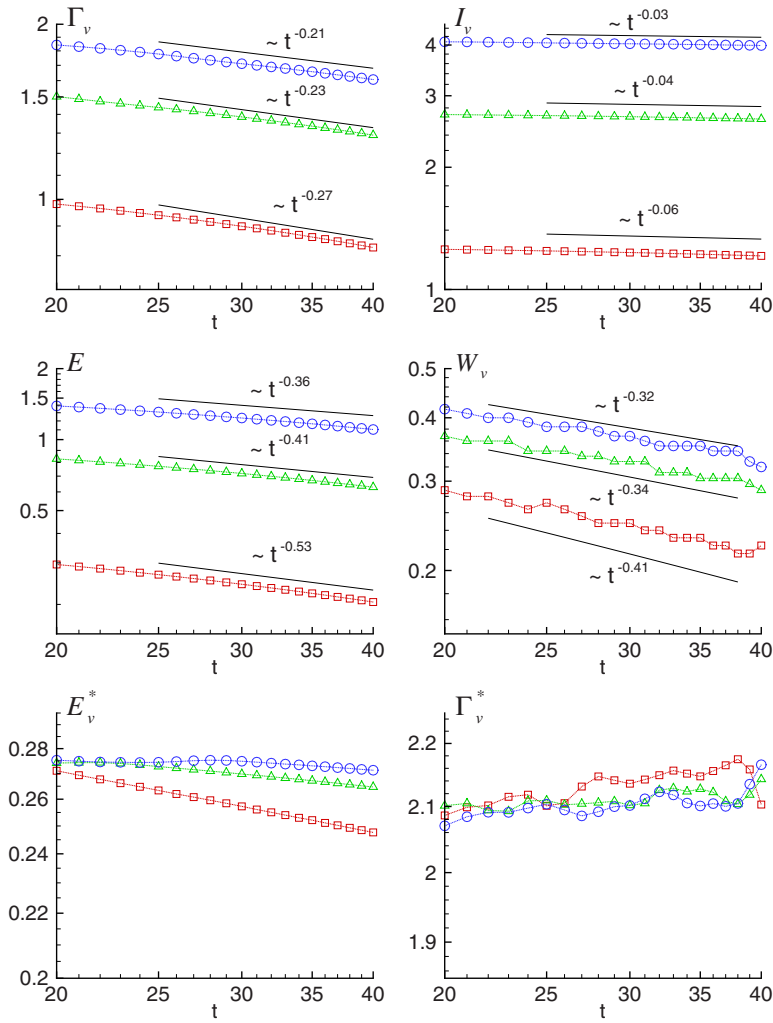
FIG. 8. (Color online) Evolution of main integrals of motion and corresponding power-law fit. Simulations for Re=1400 and different stroke ratios $L_p/D_p=6$ (○), $L_p/D_p=4$ (△), and $L_p/D_p=2$ (□).

The postprocessing program was tested by reconstructing on the present computational grid the velocity field corresponding to Hill's spherical vortex of similar size as simulated vortex rings. The errors in computing the known values (e.g., Saffman[8]) for Γ_v, I_v, and E_v were 5×10^{-6}, 2×10^{-4}, and 4×10^{-4}, respectively. We remind that the normalized energy and circulation for Hill's vortex are $E^*_{\text{Hill}}=0.16$, $\Gamma^*_{\text{Hill}}=2.7$.

Figure 8 displays the evolution of the integrals of motion (Γ_v, I_v, E_v), the translation velocity (W_v) and normalized energy (E^*_v) and circulation (Γ^*_v) of the vortex ring. The decay of each quantity is estimated by a least squares fit to power laws of the form t^p. We recall that the time t is measured relative to the beginning of the injection, as in experiments of DG. The exponents of the power-law fits shown in the figure are summarized in Table II. Very good agreement with

TABLE II. Exponents p for the power laws t^p describing the main integrals of motion (see also Fig. 8).

L_p/D_p	Γ_v	I_v	E_v	W_v	E^*_v	Γ^*_v
2	−0.27	−0.06	−0.57	−0.43	−0.13	0.04
4	−0.23	−0.04	−0.43	−0.34	−0.06	0.01
6	−0.21	−0.03	−0.36	−0.32	−0.03	0.01

the results reported by DG is observed for the stroke ratio $L_p/D_p=4$: we obtain a −0.23 power-law decay for the circulation Γ_v and a −0.34 power-law decay for the translation velocity W_v, values very close to experimental ones: −0.27 for the circulation and −0.34 for the velocity (see Figs. 7 and 8 from DG). Similar exponents for the power-law fits are obtained for the case $L_p/D_p=6$, not considered in experiments. The integral quantities decay slightly faster for the smallest stroke ratio $L_p/D_p=2$, but still at comparable rates: we obtain a −0.27 power-law exponent for Γ_v and −0.43 for W_v, compared to the values of −0.07 and, respectively, −0.37 reported by DG.

A striking feature of the postformation evolution of the vortex ring is the fact that nondimensional energy and circulation vary very slowly during this phase. The normalized energy E^*_v decays at a low rate for $L_p/D_p=2$ and is practically constant for $L_p/D_p=4$ and 6. For the three stroke ratios, the normalized circulation slowly oscillates around the value $\Gamma^*_v\approx2.1$, consistent with previously obtained values from theoretical modeling[18] ($1.77<\Gamma^*_v<2.07$) and numerical simulations[17] ($\Gamma^*_v\approx2$).

Oscillations in the variation of Γ^*_v are due to the slow rotation of the noncircular core of the vortex ring that slightly affect the measure of the translational velocity W_v. This phenomenon was also observed in experiments of DG.
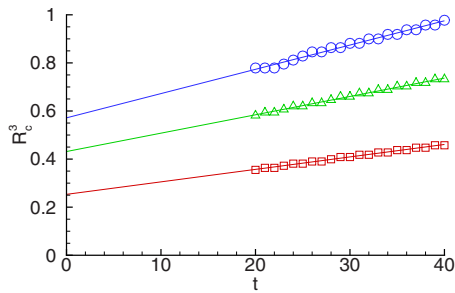
FIG. 9. (Color online) Determination of the virtual origin t_0 from the time variation of R_c^3. Simulations for different stroke ratios: $L_p/D_p=6$ ($\bigcirc$), $L_p/D_p=4$ ($\triangle$), and $L_p/D_p=2$ ($\square$).

It is important to observe from Fig. 8 and Table II that the impulse I_v of the vortex ring decays at very small rates. Note also that these decaying rates are consistent with the dimensional analysis of DG resulting in the estimation $I_v \sim \Gamma_v^3/W_v^2$. This observation suggests that the main hypothesis in the analysis of Maxworthy,[5] considering a constant impulse vortex ring, is verified in our simulations to a fair degree of approximation. This might raise the question of whether there is a discrepancy between the power-law exponents experimentally measured by DG and the higher values theoretically predicted by Maxworthy. The answer comes from the different mathematical forms of the power laws used in these studies. Maxworthy used power laws of the form $(t-t_0)^p$, with t_0 defined as a virtual origin. In order to estimate the value of t_0, Maxworthy plotted the time variation of the third power of the vortex ring radius (R_c^3), quantity considered as a characteristic dimension of the vortex bubble. Using a linear fit of $R_c^3(t)$, the value of t_0 was extrapolated as the intersection point with the time axis (see Fig. 6 from Maxworthy[5]).

We apply the same analysis to our numerical data. Figure 9 shows that the curve $R_c^3(t)$ is reasonably approximated by a linear fit for all considered stroke ratios. The virtual origin coordinate t_0 can be easily computed as the intersection point of the linear fit with the time axis. The values are compiled in Table III. Notice that the values of t_0 are practically identical for the largest stroke ratios, $L_p/D_p=4$ and 6. The exponents p of the power laws $(t-t_0)^p$ are calculated from Fig. 8 and displayed in Table III. The main results of Maxworthy are remarkably recovered: the measured −1 power law for the translational velocity W_v and the predicted −2/3 power-law decay for the vortex circulation. The same decay rate for the circulation was obtained from numerical data by James and Madnia[23] when using an appropriate estimation of the virtual origin. Therefore, we can conclude

from our numerical simulations that there is no major discrepancy between the exponents of the power laws recently reported by DG and those predicted by Maxworthy in 1972.

Nevertheless, it is prudent to remember that the virtual origin model is a purely mathematical description of the vortex ring evolution that has some physical inconsistencies. Maxworthy's theory is based on his experimental results[5] showing an exponential decay of the translation velocity with the downstream position of the vortex ring,

$$W(Z_c) = \frac{dZ_c}{dt} = W_0 \exp\left(\frac{Z_c}{W_0 t_0}\right), \qquad (10)$$

where $W_0=W(0)$ and $-\infty < t_0 < 0$ is the negative virtual origin. This assertion was recently confirmed by experimental measurements of Scase et al.[33] Integrating Eq. (10) with the condition $Z_c(0)=0$ results in

$$Z_c(t) = -W_0 t_0 \ln\left(1 - \frac{t}{t_0}\right), \qquad (11)$$

and, finally, Maxworthy's −1 power-law decay for the translational velocity is recovered,

$$W(t) = \frac{-W_0 t_0}{t - t_0}. \qquad (12)$$

From Eqs. (11) and (12) we infer that the virtual origin location is $Z_c(t_0)=-\infty$ and the translation velocity at this point is infinite. An infinite number of vortex ring trajectories are mathematically possible to get from the virtual origin ($t=t_0$, $Z_c=-\infty$, $W=\infty$) to the cylinder lip ($t=0$, $Z_c=0$, $W=W_0$), but all are physically incorrect since the vortex ring has to travel over an infinite distance in a finite time. Besides, the physical interpretation of the constant W_0 of the model is subject to caution since at $t=0$ the vortex ring is not yet formed.

In conclusion, Maxworthy's theory is to be regarded as a mathematical model using two parameters (W_0, t_0) to describe the vortex ring evolution. The imagined vortex ring is forced to pass the cylinder lip with the correct values of circulation, impulse, radial size, and translation velocity. This model is required by the experimental evidence[5,33] of the exponential decay equation (10) of the translation velocity with the downstream position of the vortex ring. As stated in the original paper of Maxworthy, this is rather unusual, compared to the cases of jets, plumes, etc., in which an algebraic variation of all quantities with distance is observed. The exponential decay law (10) is also verified by our numerical data, as shown in Fig. 10. Solid lines in the graph represents the theoretical law (10) with constants (W_0, t_0) calculated by a nonlinear fit. It is interesting to note from Fig. 10 that the value of W_0 is close to the value $W_p/2 = 0.5$, used in analytical models[18,24] to approximate the translation velocity of the vortex ring. We have also checked that the values of the virtual time origin obtained from this fit are consistent with those displayed in Table III (e.g., $t_0=-55.16$ for $L_p/D_p=4$ and $t_0=-63.66$ for $L_p/D_p=6$) and do not significantly affect the scaling law exponents in the same table.

The last point that needs to be discussed here is Maxworthy's assumption of constant bubble impulse. Using the

TABLE III. Exponents p for the power laws $(t-t_0)^p$ describing the main integrals of motion. The value of the virtual origin t_0 is calculated from Fig. 9.

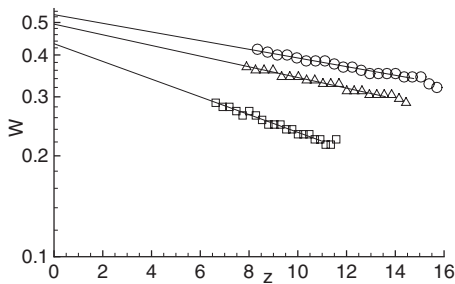| L_p/D_p	t_0	Γ_v	I_v	E_v	W_v	E_v^*	Γ_v^*
2	−48.85	−0.66	−0.15	−1.36	−1.01	−0.29	0.06
4	−56.51	−0.65	−0.12	−1.20	−0.97	−0.16	0.04
6	−56.63	−0.60	−0.09	−1.01	−0.93	−0.06	0.05

FIG. 10. Verification of the exponential decay equation (10) of the translation velocity with the downstream position of the vortex ring. Plot using semilogarithmic axis for $L_p/D_p=6$ (○), $L_p/D_p=4$ (△), and $L_p/D_p=2$ (□).

virtual origin model results in larger exponents in the power-law decay of the impulse, as shown in Table III compared to Table II. However, the decay rate of the impulse remains very slow (around a $-1/10$ power-law decay) and, for the considered time interval, the total variation of the impulse does not exceed 2.5% for all stroke ratios. This reduced loss of impulse explains why the model of Maxworthy is still satisfactory. Finally, we remind that the impulse considered in Tables III and II is computed using the vortex core (Ω_c) as integration domain. Integrating the nontruncated vorticity over the larger domain Ω_b (see Fig. 7) resulted in similar decaying power laws for the vortex bubble impulse. In exchange, the impulse of the domain including the vortex bubble and its wake remains remarkably constant. This suggests that the impulse is continuously transferred from the bubble to the wake, as described in Maxworthy's theory.

C. Fit to ideal vortex ring models

Matching numerically or experimentally generated vortex rings to ideal vortex models is useful in theoretical analysis predicting properties of practical interest such as the formation number.[4,18,19,21] We consider in this section two classes of vortex ring models: the largely used Norbury–Fraenkel[6,7] vortex family (see also Shariff and Leonard[1]) and the recent model proposed by Kaplanski and Rudi.[4] The vortex ring numerically obtained for $L_p/D_p=4$ at $t=30$ (see Figs. 4 and 7) will be matched to these two models. The details of the fitting procedures are explained in the Appendix. We present in the following the main characteristics of the ideal vortex models (hereinafter denoted as NF and, respectively, KR vortex) and analyze their relevance in describing numerically generated vortex rings.

Norbury[6] numerically calculated the properties of a class of inviscid vortex rings with vorticity distribution proportional to the distance to the axis of symmetry. The vortices of this family are identified by a single geometric parameter α, which is the nondimensional mean core radius,

$$\alpha = \frac{\sqrt{|\Omega_c|/\pi}}{R_c}. \tag{13}$$

For $\alpha \to 0$, the classical thin-core vortex[8] is recovered, while Hill's spherical vortex is included at the upper bound ($\alpha = \sqrt{2}$). Norbury calculated the shape of the vortex core and vortex bubble, the integrals of motion of the vortex ring for

different values of the parameter α and presented the results in tabular form. Analytical expressions of these quantities were proposed by Fraenkel[7] for $\alpha \to 0$ and Norbury[6] for $\alpha \to \sqrt{2}$. This model is easy to use in practice since the calculation of the parameter α needs as input only the normalized energy E_v^* of the real vortex ring. The value of α allows to compute all remaining characteristic scales of the vortex from tabulated values (see the Appendix for details and a discussion).

Kaplanski and Rudi[4] have recently proposed a more realistic class of ideal vortex rings. The vorticity in the core is Gaussian and a viscous (diffusive) length scale ℓ is introduced. This class of vortex rings, that can be considered as the viscous analog to NF vortices, is also identified by a single geometric parameter $\tau = R_c/\ell$. The matching procedure also starts by calculating τ using as input the normalized energy E_v^*; the integrals of motion are then calculated from somewhat cumbersome analytical expressions (see the Appendix for details).

The simulated vortex ring ($L_p/D_p=4$, $t=30$) has the normalized energy $E_v^*=0.27$ and normalized circulation $\Gamma_v^* =2.1$. It is useful to remember that these values vary slowly (of 4% maximum) during the postformation phase (see Fig. 8). The corresponding fits using as input the value of E_v^* give the following values for the main parameters: $\alpha=0.6$ for the NF vortex and $\tau=3.48$ for the KR vortex. We first note that the equivalence between the two classes of vortices suggested by Kaplanski and Rudi[4] is not valid in this case. They proposed to approximate the area of the vortex core as $|\Omega_c| =\pi\ell^2$, obtaining from Eq. (13) that $\tau=1/\alpha$. This is manifestly not the case for our example.

The complete comparison between the simulated vortex and the resulting fits to ideal models is displayed in Fig. 11. The vorticity and streamline fields were numerically reconstructed for each vortex model. We should emphasize the fact that the fitted vortices have the same circulation Γ_v and impulse I_v as the simulated vortex. This determines the geometrical characteristics of the vortex models: the vortex ring radius R_c is calculated by the fitting procedure, while the axial coordinate Z_c is imposed for all vortices.

As expected, normalized vorticity isocontours [Figs. 11(a)–11(c)] are circular (quasi-Gaussian vorticity distribution) for the KR vortex and straight (linear vorticity distribution) for the NF vortex. It is useful to extract radial vorticity profiles at $z=Z_c$ in order to determine the exact position of the vortex center. Figure 12 shows that the KR vortex has realistic vorticity distribution. The vorticity peak is slightly larger than for the simulated vortex and shifted toward the symmetry axis. This sets the vortex radius at a lower value ($R_c^{KR}=0.78$) compared to simulated vortex ($R_c=0.87$).

The linear vorticity distribution in the NF vortex allows to define only a geometrical vortex center, as the midpoint of the radial extent of the core. We obtain from Fig. 12 the value $R_c^{NF}=0.72$. It is interesting to note that applying the same definition to the simulated vortex results in a very close value, $\bar{R}_c=0.71$. The fact that the NF and simulated vortices have the same geometrical center is also visible in Fig. 11(g) showing the contours $\delta\Omega_c$ of vortex cores. The core of the
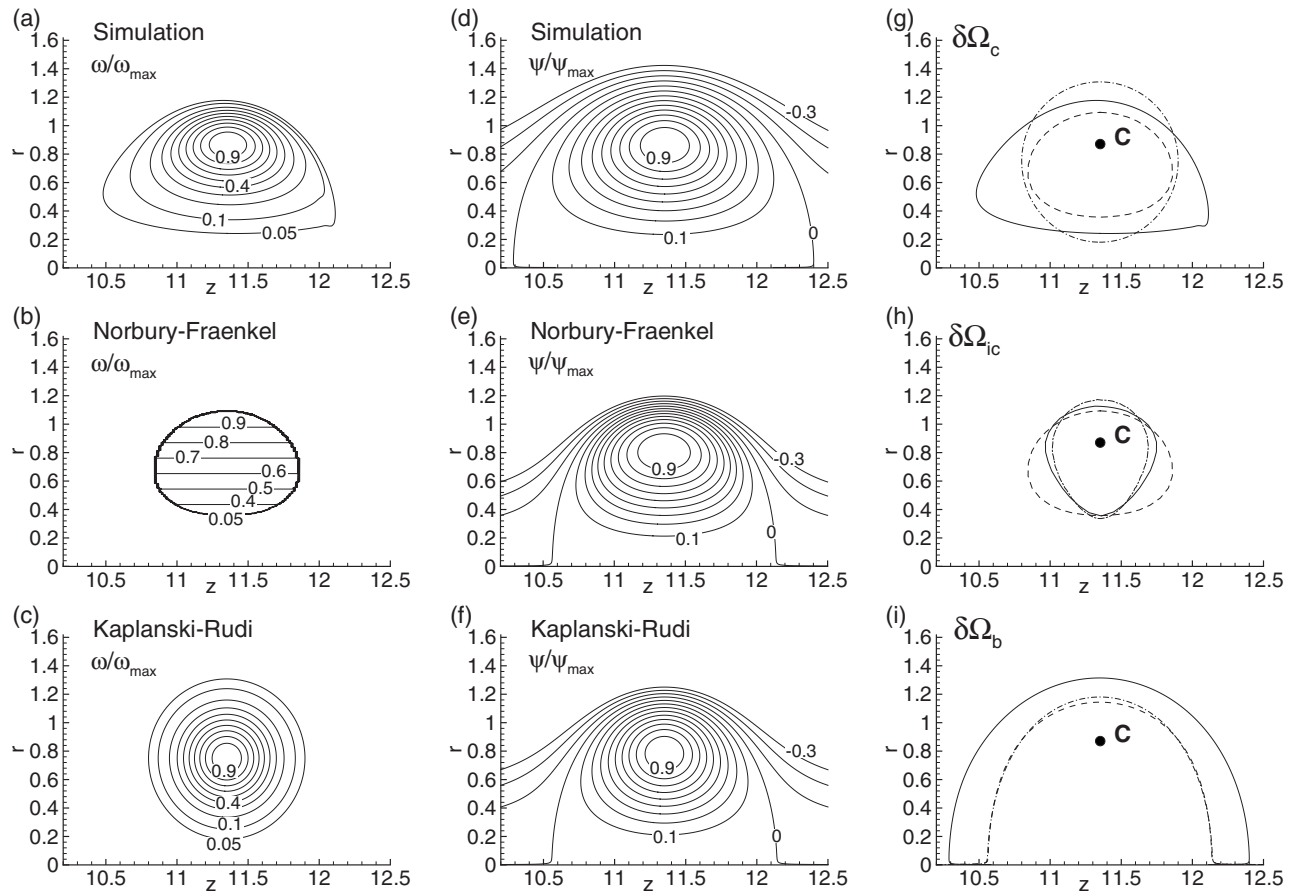
FIG. 11. Fit of the vortex numerically obtained for $L_p/D_p=4$, $t=30$ to ideal models of Norbury and Fraenkel and of Kaplanski and Rudi. Isocontours of the normalized vorticity $\tilde{\omega}=\omega/\omega_{max}$ [(a)–(c)] and isocontours of the normalized stream function ψ_{vr}/ψ_{max} [(d)–(f)]. Boundary contours of the vortex core (g), vortex inner core (h), and vortex bubble (i) for the simulated vortex ring (solid line), Norbury–Fraenkel fit (dashed line) and Kaplanski–Rudi fit (dash-dotted line). The center C of the simulated vortex is also represented.

NF vortex is elongated in the axial direction, as for the simulated vortex, while the core of the KR vortex is circular. Since the circulation is the same, the different vorticity distribution accounts for the larger core area of the KR vortex ($|\delta\Omega_c^{KR}|/|\delta\Omega_c|=0.80$) compared to the NF vortex ($|\delta\Omega_c^{NF}|/|\delta\Omega_c|=0.52$). Another demonstration of the more realistic vorticity distribution in the KR vortex is offered by the contours $\delta\Omega_{ic}$ of the inner core shown in Fig. 11(h). The KR vortex and the simulated vortex have similar inner cores, while for the NF vortex the core and the inner core are identical.
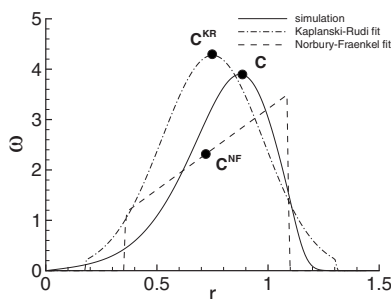

FIG. 12. Fit to ideal vortex models. Radial vorticity profiles through the center C ($z=Z_c$) of the vortex ring. Identification of vortex centers C.

The main argument used in theoretical studies[17,21] to justify matching of experimentally or numerically generated vortices to NF vortices was the similarity of the streamlines. In order to verify this assumption, we compute from Eqs. (8) and (9) the instantaneous streamlines in the frame of reference translating with the vortex. Figures 11(d)–11(f) show qualitatively similar streamlines for the three vortices. For a more quantitative comparison we separate in Fig. 11(i) the dividing streamline ($\psi_{vr}=0$) bounding the vortex bubble $\delta\Omega_b$. Surprisingly, the bubbles of NF and KR vortices are practically the same. The volume of the bubble, representing the volume of fluid carried with the vortex ring, is underestimated by 40%. This could be a drawback of both models when estimating quantities of practical interest as the fluid entrainment in the vortex ring.[3]

A final quantitative assessment of the streamline distribution is provided by calculating the vortex ring signature $V(\psi_{vr})$ introduced by Moffatt[34] to identify a vortex ring without swirl. This topological invariant is defined as the volume inside the torus $\psi_{vr}=$cst. [$V(0)$ is the volume of the vortex bubble]. Figure 13 shows that the normalized signature $V(\psi_{vr})/V(0)$ allows to identify the numerically generated vortex ring since it is invariant during the entire postformation phase. As a consequence of the more realistic vorticity distribution, the KR vortex has a signature closer to that of
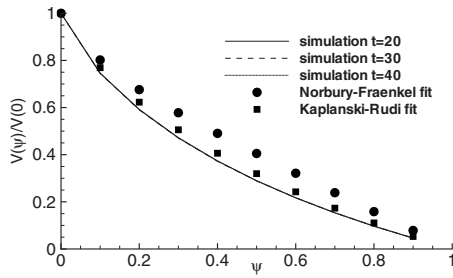
FIG. 13. Fit to ideal vortex models. Signature (Ref. [34]) of the vortex ring normalized by its maximum value.

the simulated vortex than the NF vortex. Similar qualitative and quantitative results were obtained for the fit of vortex rings generated for the other two stroke ratios ($L_p/D_p = 2$ and 6).

IV. SUMMARY

Direct numerical simulations of an axisymmetric laminar vortex ring generated by a piston/cylinder arrangement have been performed using an incompressible Navier–Stokes solver in cylindrical coordinates. The Reynolds number of the flow (Re=1400) and the piston stroke ratios ($L_p/D_p = 2, 4, 6$) were prompted by recent experiments of Dabiri and Gharib.[3] Numerical results are first validated for the formation phase. Good agreement with existing numerical[16] and experimental[12] data is obtained. The main body of the paper focuses then on the postformation phase of the vortex ring by considering long time simulations.

Two main diagnostics are considered in this study in order to characterize the postformation vortex ring: the scaling laws of the integrals of motion (circulation, impulse, energy) and the topological structure of the vortex. The two are related since the calculation of the integrals of motion requires to separate the vortex core from the vortex wake flow by truncating the vorticity field. We show that extracting the vortex inner core[32] provides an objective method in setting the upper value for the cutoff vorticity level. The vortex structure is then completely described by calculating the embedded boundaries of the vortex inner core, vortex core, and vortex bubble. This topology is found to be remarkably self-similar during the entire postformation phase. Concerning the scaling laws of the integrals of motion, the present study dissipates the apparent discrepancy between the recent experimental results of Dabiri and Gharib[3] and theoretical predictions of Maxworthy.[5] We show that the exponents of the power laws depend on whether or not the virtual time origin proposed by Maxworthy is used. In this way our numerical data become consistent with both studies.

We finally address in detail the question of how to fit computationally or experimentally vortex rings to ideal vortex models. Two classes of vortex ring models are considered: the largely used Norbury–Fraenkel[6,7] inviscid vortex family and the recent viscous model proposed by Kaplanski and Rudi.[4] Although the linear vorticity distribution in the Norbury–Fraenkel vortex is far from being realistic, matching the simulated vortex to this model provides not only a good prediction of the normalized quantities as already

shown in the literature, but also a good estimation of individual integrals of motion, such as circulation or impulse.

The realistic (Gaussian) vorticity distribution in the Kaplanski–Rudi model offers, in addition to a good prediction of integral quantities, a more accurate description of the vortex ring topology when comparing the contours of inner cores or calculating the vortex signatures.[34] Nevertheless, it is prudent to note that both models underestimate the volume of fluid carried inside the vortex bubble by 40%. This could be a drawback in practical applications requiring an estimate of the flow entrainment. An improved Kaplanski–Rudi model taking into account the oblate ellipsoid shape of the real ring could eventually overcome this difficulty.

ACKNOWLEDGMENTS

APPENDIX: FITTING TO IDEAL VORTEX RING MODELS

We present in this appendix the details of the procedures used to fit the numerically simulated vortex rings to ideal vortex models. We use as a reference case the vortex obtained for $L_p/D_p = 4$ at $t = 30$ (see Figs. 4 and 7), described by the following quantities:

$$\Gamma_v = 1.38, \quad I_v = 2.66, \quad E_v = 0.73,$$

$$E_v^* = 0.27, \quad \Gamma_v^* = 2.1, \quad W_v = 0.32.$$

We consider in the following that the density of the fluid is $\rho = 1$.

1. Nobury–Fraenkel model

The vorticity distribution in a Norbury–Fraenkel vortex is linear, proportional to the distance to the axis of symmetry,

$$\omega = \Omega r. \tag{A1}$$

The other two parameters characterizing the vortex are the ring radius R_c of the vortex ring and the geometric parameter α defined by Eq. (13). The main physical quantities are calculated following the expressions[6]

$$\Gamma = \Omega R_c^3 \alpha^2 \, \Gamma_{NF}(\alpha), \tag{A2}$$

$$I = \Omega R_c^5 \alpha^2 \, I_{NF}(\alpha), \tag{A3}$$

$$E = \Omega^2 R_c^7 \alpha^4 \, E_{NF}(\alpha), \tag{A4}$$

$$W = \Omega R_c^2 \alpha^2 \, W_{NF}(\alpha), \tag{A5}$$

where nondimensional quantities $()_{NF}$ are given in tabular form. Useful asymptotic expressions are given by Fraenkel[7] for $\alpha \to 0$ (thin vortices),
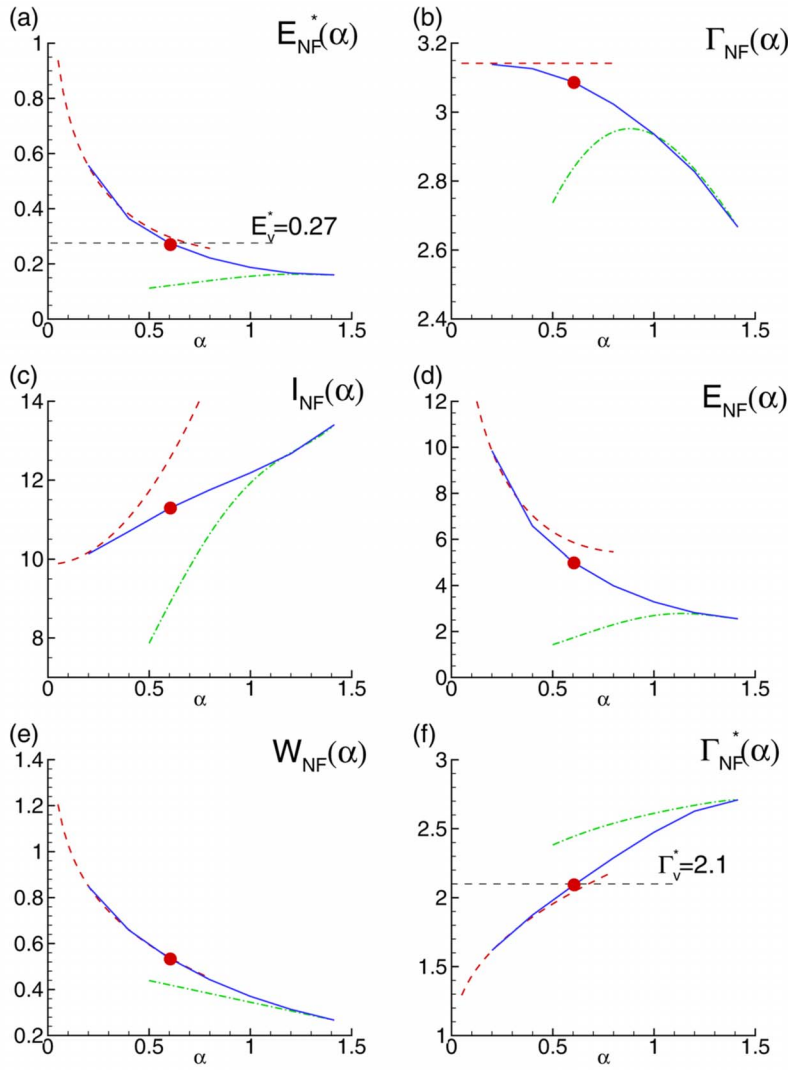
$$\Gamma_{NF}(\alpha) = \pi, \tag{A6}$$

FIG. 14. (Color online) Norbury–Fraenkel ideal vortex model. Variation of the nondimensional quantities ()$_{\mathrm{NF}}$ with the parameter α. Numerical tabulated values from Norbury (Ref. [6]) (solid line), asymptotic approximations of Fraenkel (Ref. [7]) (dashed line) and Norbury (Ref. [6]) (dash-dotted line). The points represent values corresponding to the simulated vortex ring for L_p/D_p =4 at $t=30$.

$$I_{\mathrm{NF}}(\alpha) = \pi^2\left(1 + \frac{3}{4}\alpha^2\right), \tag{A7}$$

$$E_{\mathrm{NF}}(\alpha) = \pi^2\left[\frac{1}{2}\ln\left(\frac{8}{\alpha}\right) - \frac{7}{8} + \frac{3}{16}\alpha^2\ln\left(\frac{8}{\alpha}\right)\right], \tag{A8}$$

$$W_{\mathrm{NF}}(\alpha) = \frac{1}{4}\ln\left(\frac{8}{\alpha}\right) - \frac{1}{16} + \alpha^2\left[-\frac{3}{32}\ln\left(\frac{8}{\alpha}\right) + \frac{15}{128}\right], \tag{A9}$$

and Norbury[6] for $\alpha \to \sqrt{2}$ (thick vortices),

$$\Gamma_{\mathrm{NF}}(\alpha) = \frac{1}{3}a^3\left[1 + \sqrt{2}\bar{\alpha} - \frac{3}{16}\bar{\alpha}^2\ln\left(\frac{8\sqrt{2}}{\bar{\alpha}}\right) + 1.69\bar{\alpha}^2\right], \tag{A10}$$

$$I_{\mathrm{NF}}(\alpha) = \frac{2\pi}{15}a^5\left[1 + \sqrt{2}\bar{\alpha} + \frac{141}{64}\bar{\alpha}^2\right], \tag{A11}$$

$$E_{\mathrm{NF}}(\alpha) = \frac{2\pi}{315}a^7\left[1 + 2\sqrt{2}\bar{\alpha} + \frac{383}{64}\bar{\alpha}^2\right], \tag{A12}$$

$$W_{\mathrm{NF}}(\alpha) = \frac{2}{15}a^2, \tag{A13}$$

where $\bar{\alpha} = \sqrt{2} - \alpha$ and $a = 2(1 - \bar{\alpha}/2\sqrt{2})$.

The generally used[19,35] fitting procedure is based on Fraenkel's expressions. From Eqs. (A6)–(A8) the normalized energy $E^* = E/(I^{1/2}\Gamma^{3/2})$ can be obtained as a function of the single parameter α. Solving the nonlinear equation $E^* = E_v^*$ will then give the value of α. However, Fraenkel's asymptotic expressions can be used with reasonable accuracy only for $\alpha \lesssim 0.5$, as shown in Fig. 14. For intermediate values of the parameter α is better to use numerical tabulated values. Norbury's expansions (A10)–(A13) are limited for $1 \leqslant \alpha \leqslant \sqrt{2}$.

We use the following fitting procedure based on numerical tabulated values from Norbury[6] (note that we have to extract three parameters from four equations).

- The value of the normalized energy $E^* = E_v^*$ is used to interpolate from Fig. 14(a) the parameter α; all nondimensional quantities ()$_{\mathrm{NF}}$ are then interpolated from Figs. 14(b)–14(e).
- We impose the values of the dimensional circulation

Γ_v and impulse I_v and calculate from Eqs. (A2) and (A3) the remaining parameters of the model,

$$R_c = \sqrt{\frac{I_v}{I_{NF}}\frac{\Gamma_{NF}}{\Gamma_v}}, \quad \Omega = \frac{\Gamma_v}{\Gamma_{NF}}\frac{1}{R_c^3 \alpha^2}. \tag{A14}$$

- We check the accuracy of the model by calculating from Eqs. (A4) and (A5) the values of the dimensional energy E, translation velocity W, and, finally, normalized circulation Γ^*.

Figure 14 also shows the points resulting from the fitting procedure. The ideal vortex is characterized by $\alpha=0.605$, $R_c=0.724$, and $\Omega=3.215$. The values of the dimensional circulation and impulse are exactly fitted. The model predicts the values of the dimensional energy, translation velocity, and normalized circulation with relative errors of 0.01% and, respectively, 3% and 2%. Test of different fitting procedures (starting from the value of the normalized circulation or using Fraenkel's expansions) resulted in slightly larger relative errors, in particular, for the translation velocity.

2. Kaplanski–Rudi model

The parameters describing a Kaplanski–Rudi vortex[4] of given impulse I are the vortex ring radius R_c, the diffusivity scale of the ring's core ℓ, and the vorticity amplitude Ω. A vortex from this family is identified by the ratio $\tau=R_c/\ell$. The vorticity distribution is Gaussian,

$$\omega = \Omega \exp\left[-\tfrac{1}{2}(\sigma^2 + \eta^2 + \tau^2)\right]\mathbf{I}_1(\sigma\tau), \tag{A15}$$

where $\sigma=r/\ell$, $\eta=[z-Z_c(t)]/\ell$, and Z_c the axial coordinate of the vortex center. Analytical expression are obtained[4] for the circulation,

$$\Gamma = \Gamma_0\left[1 - \exp\left(-\frac{\tau^2}{2}\right)\right], \quad \Gamma_0 = \frac{I}{\pi R_c^2}, \tag{A16}$$

energy,

$$E = \frac{I^2}{2\pi^2}\frac{\tau}{R_c^3}\left[\frac{1}{12}\sqrt{\pi}\tau^2 {}_2F_2\left(\left\{\frac{3}{2},\frac{3}{2}\right\},\left\{\frac{5}{2},3\right\},-\tau^2\right)\right], \tag{A17}$$

and translation velocity,

$$W = \frac{I}{4\pi^2}\frac{\tau}{R_c^3}\left\{3\sqrt{\pi}\exp\left(-\frac{\tau^2}{2}\right)\mathbf{I}_1\left(\frac{\tau^2}{2}\right)\right.$$
$$+ \frac{1}{12}\sqrt{\pi}\tau^2 {}_2F_2\left(\left\{\frac{3}{2},\frac{3}{2}\right\},\left\{\frac{5}{2},3\right\},-\tau^2\right)$$
$$\left. - \frac{3}{5}\sqrt{\pi}\tau^2 {}_2F_2\left(\left\{\frac{3}{2},\frac{5}{2}\right\},\left\{2,\frac{7}{2}\right\},-\tau^2\right)\right\}. \tag{A18}$$

In previous expressions $\mathbf{I}_1$ is the first-order modified Bessel function and ${}_2F_2$ the generalized hypergeometric function. The fitting procedure consists in the following steps.

- Combining the relations (A17) and (A16) we obtain an expression of the normalized energy $E^*=E/(I^{1/2}\Gamma^{3/2})$ depending only on the parameter τ; solving the non-

linear equation $E^*=E_v^*$ gives the value of the parameter τ.
- Matching $\Gamma=\Gamma_v$ and $I=I_v$ in Eq. (A16) allows to calculate Γ_0 and the vortex radius $R_c=\sqrt{I/(\pi\Gamma_0)}$.
- The viscous scale results immediately, $\ell=R_c/\tau$, and the vorticity amplitude is calculated as[4]

$$\Omega = \frac{2I_v}{(2\pi)^{3/2}R_c\ell^3}. \tag{A19}$$

- The translation velocity is finally calculated from Eq. (A18).

The fitting procedure for our example vortex gives $\tau=3.48$, $R_c=0.781$, $\ell=0.225$, $\Omega=38.21$, and $W=0.293$. The translation velocity and normalized energy are approximated with a relative error of 8%.

[1] K. Shariff and A. Leonard, "Vortex rings," Annu. Rev. Fluid Mech. **24**, 235 (1992).

[2] T. T. Lim and T. B. Nickels, "Vortex rings," in *Vortices in Fluid Flows*, edited by S. I. Green (Kluwer, Dordrecht, 1995), p. 95.

[3] J. O. Dabiri and M. Gharib, "Fluid entrainment by isolated vortex rings," J. Fluid Mech. **511**, 311 (2004).

[4] F. B. Kaplanski and Y. A. Rudi, "A model for the formation of 'optimal' vortex ring taking into account viscosity," Phys. Fluids **17**, 087101 (2005).

[5] T. Maxworthy, "The structure and stability of vortex rings," J. Fluid Mech. **51**, 15 (1972).

[6] J. Norbury, "A family of steady vortex rings," J. Fluid Mech. **57**, 417 (1973).

[7] L. E. Fraenkel, "Examples of steady vortex rings of small cross-section in an ideal fluid," J. Fluid Mech. **51**, 119 (1972).

[8] P. G. Saffman, *Vortex Dynamics*, Cambridge Monographs on Mechanics and Applied Mathematics (Cambridge University Press, Cambridge, 1992).

[9] D. G. Akhmetov, "Formation and basic parameters of vortex rings," J. Appl. Mech. Tech. Phys. **42**, 794 (2001).

[10] J. P. Sullivan, "Study of a vortex ring using a laser Doppler velocimeter," AIAA J. **11**, 1384 (1973).

[11] A. Weigand and M. Gharib, "On the evolution of laminar vortex rings," Exp. Fluids **22**, 447 (1997).

[12] M. Gharib, E. Rambod, and K. Shariff, "A universal time scale for vortex ring formation," J. Fluid Mech. **360**, 121 (1998).

[13] S. Krueger, J. O. Dabiri, and M. Gharib, "Vortex ring pinch-off in the presence of simultaneously initiated uniform background co-flow," Phys. Fluids **15**, L49 (2003).

[14] J. O. Dabiri and M. Gharib, "Starting flow through nozzles with temporally variable exit diameter," J. Fluid Mech. **538**, 111 (2005).

[15] M. Rosenfeld, E. Rambod, and M. Gharib, "Circulation and formation number of a laminar vortex ring," J. Fluid Mech. **376**, 297 (1998).

[16] W. Zhao, H. F. Steven, and L. G. Mongeau, "Effects of trailing jet instability on vortex ring formation," Phys. Fluids **12**, 589 (2000).

[17] K. Mohseni, H. Ran, and T. Colonius, "Numerical experiments on vortex ring formation," J. Fluid Mech. **430**, 267 (2001).

[18] K. Mohseni and M. Gharib, "A model for universal time scale of vortex ring formation," Phys. Fluids **10**, 2436 (1998).

[19] M. Shusser and M. Gharib, "Energy and velocity of a forming vortex ring," Phys. Fluids **12**, 618 (2000).

[20] K. Mohseni, "Statistical equilibrium theory for axisymmetric flow: Kelvin's variational principle and an explanation for the vortex ring pinch-off process," Phys. Fluids **13**, 1924 (2001).

[21] P. F. Linden and J. S. Turner, "The formation of 'optimal' vortex rings, and the efficiency of propulsion devices," J. Fluid Mech. **427**, 61 (2001).

[22] T. Maxworthy, "Some experimental studies of vortex rings," J. Fluid Mech. **81**, 465 (1977).

[23] S. James and C. K. Madnia, "Direct numerical simulation of a laminar vortex ring," Phys. Fluids **8**, 2400 (1996).

[24] K. Mohseni, "A formulation for calculating the translational velocity of a vortex ring or pair," Bioinspiration & Biomimetics **1**, S57 (2006).

[25] R. Verzicco and P. Orlandi, "A finite-difference scheme for three-

dimensional incompressible flows in cylindrical coordinates," J. Comput. Phys. **123**, 402 (1996).

[26] P. Orlandi, *Fluid Flow Phenomena: A Numerical Toolkit* (Kluwer Academic, Dordrecht, 1999).

[27] J. Kim and P. Moin, "Application of a fractional step method to incompressible Navier–Stokes equations," J. Comput. Phys. **59**, 308 (1985).

[28] R. Sau and K. Mahesh, "Passive scalar mixing in vortex rings," J. Fluid Mech. **582**, 449 (2007).

[29] A. Michalke, "Survey on jet instability theory," Prog. Aerosp. Sci. **21**, 159 (1984).

[30] I. Orlanski, "A simple boundary condition for unbounded hyperbolic flows," J. Comput. Phys. **21**, 251 (1976).

[31] M. R. Ruith, P. Chen, and E. Meiburg, "Development of boundary conditions for direct numerical simulations of three-dimensional vortex breakdown phenomena in semiinfinite domains," Comput. Fluids **33**, 1225 (2004).

[32] P. G. Saffman, "The number of waves on unstable vortex rings," J. Fluid Mech. **84**, 625 (1978).

[33] M. M. Scase and S. B. Dalziel, "An experimental study of the bulk properties of vortex rings translating through a stratified fluid," Eur. J. Mech. B/Fluids **25**, 302 (2006).

[34] H. K. Moffatt, "Generalised vortex rings with and without swirl," Fluid Dyn. Res. **3**, 22 (1988).

[35] M. Shusser, M. Gharib, M. Rosenfeld, and K. Mohseni, "On the effect of pipe boundary layer growth on the formation of a laminar vortex ring generated by a piston-cylinder arrangement," Theor. Comput. Fluid Dyn. **15**, 303 (2002).